

GRB 051022: PHYSICAL PARAMETERS AND EXTINCTION OF A PROTOTYPE DARK BURST

EVERT ROL,¹ ALEXANDER VAN DER HORST,² KLAAS WIERSEMA,² SANDEEP K. PATEL,^{3,4} ANDREW LEVAN,⁵
MELISSA NYSEWANDER,⁶ CHRYSSE KOUVELIOTOU,^{3,7} RALPH A. M. J. WIJERS,² NIAL TANVIR,¹
DAN REICHAERT,⁸ ANDREW S. FRUCHTER,⁶ JOHN GRAHAM,^{6,9} JAN-ERIK OVALDSEN,¹⁰
ANDREAS O. JAUNSEN,¹⁰ PETER JONKER,^{11,12,13} WILBERT VAN HAM,¹⁴
JENS HJORTH,¹⁵ RHAANA L. C. STARLING,¹ PAUL T. O'BRIEN,¹
JOHAN FYNBO,¹⁵ DAVID N. BURROWS,¹⁶ AND RICHARD STROM,^{2,17}

Received 2007 June 11; accepted 2007 July 2

ABSTRACT

GRB 051022 was undetected to deep limits in early optical observations, but precise astrometry from radio and X-rays showed that it most likely originated in a galaxy at $z \approx 0.8$. We report radio, optical, near-infrared, and X-ray observations of GRB 051022. Using the available X-ray and radio data, we model the afterglow and calculate its energetics, finding it to be an order of magnitude lower than that of the prompt emission. The broadband modeling also allows us to precisely define various other physical parameters and the minimum required amount of extinction to explain the absence of an optical afterglow. Our observations suggest a high extinction, at least 2.3 mag in the infrared (J) and at least 5.4 mag in the optical (U) in the host-galaxy rest frame. Such high extinctions are unusual for GRBs and likely indicate a geometry where our line of sight to the burst passes through a dusty region in the host that is not directly colocated with the burst itself.

Subject headings: dust, extinction — gamma rays: bursts

1. INTRODUCTION

Dark gamma-ray bursts (GRBs)—at the most basic level those without optical afterglows—are a long-standing issue in GRB observations. Although in many cases the nondetection of an afterglow at optical wavelengths may simply be due to an insufficiently deep search, or one which takes place at late times (e.g., Fynbo et al. 2001), a subset of GRBs with bright X-ray afterglows remains undetected despite prompt and deep optical searches (e.g., Groot et al. 1998) and directly implies suppression of the optical light.

There are several plausible explanations for this, the most likely being that the burst is at high redshift, such that the Ly α break has crossed the passband in question, or that there is high extinction in the direction of the GRB. Examples of both have been found, with a small number of GRBs at $z > 5$ appearing as I - and R -band dropouts (e.g., Jakobsson et al. 2006b; Haislip et al. 2006) and some GRB afterglows appearing very red at lower redshift, due to effects of extinction (e.g., Levan et al. 2006; Rol et al. 2007).

Identification of GRBs at very high redshifts is the key to using them as cosmological probes. The proportion of bursts exhibiting high dust extinction is also interesting from the point of view of estimating the proportion of star formation that is dust enshrouded, as well as understanding the environments which favor GRB production (Trentham et al. 2002; Tanvir et al. 2004).

The detection and follow-up of dark bursts at other wavelengths is essential, as it enables (1) the modeling of the afterglow, deriving estimates of the extinction and energies involved, potentially providing information about the direct burst environment, (2) pinpointing the burst position in the host, to enable late-time high-resolution imaging and the detection of dust enhanced regions in the host, and (3) determination of the properties of the GRB host itself, such as the star formation rate (SFR) and average host-galaxy extinction.

The *High Energy Transient Explorer 2* mission (*HETE-2*; Ricker et al. 2003) detected and located an unusually bright gamma-ray burst (Olive et al. 2005) with its three main instruments, the French Gamma Telescope (FREGATE), the Wide Field X-ray Monitor (WXM), and the Soft X-ray Camera (SXC), on 2005 October 22. A 2.5' localization was sent out within minutes, enabling prompt follow-up observations (e.g., Torii 2005; Schaefer 2005); a target-of-opportunity observation was also performed with *Swift*. Details of the *HETE-2* observations can be found in Nakagawa et al. (2006).

The *Swift* observations resulted in the detection of a single fading point source inside the SXC error region, which was consequently identified as the X-ray afterglow of GRB 051022 (Racusin et al.

¹ Department of Physics and Astronomy, University of Leicester, University Road, Leicester, LE1 7RH, UK; evert.rol@star.le.ac.uk.

² Astronomical Institute, University of Amsterdam, Kruislaan 403, NL-1098 SJ Amsterdam, Netherlands.

³ National Space Science and Technology Center, 320 Sparkman Drive, Huntsville, AL 35805.

⁴ Optical Sciences Corporation, 6767 Old Madison Pike, Suite 650, Huntsville, AL 35806.

⁵ Department of Physics, University of Warwick, Coventry, CV4 7AL, UK.

⁶ Space Telescope Science Institute, 3700 San Martin Drive, Baltimore, MD 21218.

⁷ NASA Marshall Space Flight Center, Huntsville, AL 35812.

⁸ Department of Physics and Astronomy, University of North Carolina at Chapel Hill, Campus Box 3255, Chapel Hill, NC 27599.

⁹ Department of Physics and Astronomy, Johns Hopkins University, 3400 North Charles Street, Baltimore, MD 21218.

¹⁰ Institute of Theoretical Astrophysics, University of Oslo, P.O. Box 1029, Blindern, N-0315 Oslo, Norway.

¹¹ SRON, Netherlands Institute for Space Research, Sorbonnelaan 2, NL-3584 CA Utrecht, Netherlands.

¹² Harvard-Smithsonian Center for Astrophysics, 60 Garden Street, Cambridge, MA 02138.

¹³ Astronomical Institute, Utrecht University, P.O. Box 80000, 3508 TA, Utrecht, Netherlands.

¹⁴ Department of Astrophysics, Radboud University Nijmegen, P.O. Box 9010, NL-6500 GL Nijmegen, Netherlands.

¹⁵ Dark Cosmology Centre, Niels Bohr Institute, University of Copenhagen, Juliane Maries Vej 30, DK-2100 Copenhagen Ø, Denmark.

¹⁶ Department of Astronomy and Astrophysics, Pennsylvania State University, University Park, PA 16801.

¹⁷ ASTRON, P.O. Box 2, NL-7990 AA Dwingeloo, Netherlands.

2005a). However, optical and near-infrared (NIR) observations failed to reveal any afterglow to deep limits, while radio and millimeter observations with the Very Large Array (VLA), the Westerbork Synthesis Radio Telescope (WSRT), and the Plateau de Bure Interferometer detected the radio counterpart (Cameron & Frail 2005; van der Horst et al. 2005; Bremer et al. 2005). The position coincides with its likely host galaxy (Berger & Wyatt 2005) at a redshift of $z = 0.8$ (Gal-Yam et al. 2005).

In this paper, we describe our X-ray, optical, NIR, and radio observations of GRB 051022. The outline of the paper is as follows: in § 2 we describe our observations, data reduction, and initial results. In § 3, we analyze these results and form our afterglow picture, which is discussed in § 4. Our findings are summarized in § 5.

In the following, we have used $F \propto \nu^{-\beta} t^{-\alpha}$ in our definition of α and β . We assume a cosmology with $H_0 = 71 \text{ km s}^{-1} \text{ Mpc}^{-1}$, $\Omega_M = 0.27$, and $\Omega_\Lambda = 0.73$. All quoted errors in this paper are 1σ (68%) errors.

2. OBSERVATIONS AND DATA REDUCTION

2.1. X-Ray Observations

X-ray observations were performed with the *Swift* X-Ray Telescope (XRT) and the *Chandra* X-Ray Observatory.

The XRT started observing the afterglow of GRB 051022 3.46 hr after the *HETE-2* trigger, for a total effective integration time of 137 ks between October 22 and November 6.

Observations were performed in Photon Counting (PC) mode, the most sensitive observing mode. We reduced the data using the *Swift* software, version 2.6, in the HEASoft package, version 6.2.0. Data were obtained from the quick-look site and processed from level 1 to level 2 FITS files using the *xrtpipeline* tool in its standard configuration. The first two orbits (until 2.1×10^4 s post-burst) show pile-up and were therefore extracted with an annular rather than circular region, with an inner radius of $19''$ and $12''$ for orbits 1 and 2, respectively, and an outer radius of $71''$. Orbits 3–7 [$(2.4\text{--}4.9) \times 10^4$ s] were extracted with a circular region of $71''$ radius, and later orbits were extracted using a $47''$ radius circle instead. The data for the light curve were extracted between channels 100 and 1000, corresponding to 1 and 10 keV, respectively; while the commonly used range is 0.3–10 keV, the large absorption prevents the detection of any data from the source below 1 keV. Otherwise, the procedure is similar to that described in Evans et al. (2007).

Observations with *Chandra* started on 2005 October 25, 21:14:20 UT, 3.34 days after the *HETE-2* trigger, for a total integration time of 20 ks (Patel et al. 2005). Data were reduced in a standard fashion with the CIAO package.

We performed astrometry by matching X-ray sources with an optical *R*-band image that was astrometrically calibrated to the 2MASS catalog. Our *Chandra* position is R.A. = $23^{\text{h}}56^{\text{m}}04.115^{\text{s}}$, decl. = $+19^{\circ}36'24.04''$ (J2000.0), with positional errors of $0.33''$ and $0.12''$ for the right ascension and declination, respectively. This puts the afterglow within $0.5''$ of the center of its host galaxy.

We modeled the XRT spectra with an absorbed power law in XSPEC (Arnaud 1996), using data from the first seven orbits. A good fit ($\chi^2/\text{dof} = 87.2/99$) was obtained with a resulting spectral energy index of $\beta = 1.00 \pm 0.12$ and excess absorption (at $z = 0.8$ and for assumed Galactic abundances) of $N_{\text{H}} = (2.82 \pm 0.46) \times 10^{22} \text{ cm}^{-2}$ on top of the estimated Galactic absorption at this position ($N_{\text{H}} = 4.06 \times 10^{20} \text{ cm}^{-2}$; Dickey & Lockman 1990). The *Chandra* data are fully in agreement with these values, showing no change in the spectrum over time between 0.3 and 3.3 days

after the burst. The absorption measured is far less than that measured by the *HETE-2* team in their prompt data, $N_{\text{H}} = (8.8_{-1.8}^{+1.9}) \times 10^{22} \text{ cm}^{-2}$ (Nakagawa et al. 2006). This could indicate a change in absorption between the early (prompt) measurements and those at the time of the XRT observations. For the prompt emission spectrum, however, the values found by Konus-*Wind* (Golenetskii et al. 2005) are rather different from those found by *HETE-2*, which may be the result of the lower energy cutoff for FREGATE compared to Konus-*Wind*. Alternatively, the fact that these spectra are an average over the whole emission period may also result in incorrect model parameters. In the two last cases, the N_{H} in the prompt emission could be as low as the XRT value and still produce an equally well fit, but with slightly different model parameters.

For the XRT data, Butler et al. (2005a) and Nakagawa et al. (2006) find a value somewhat higher than our value [4.9×10^{22} and $5.3 \times 10^{22} \text{ cm}^{-2}$ respectively, when scaled by $(1+z)^3$; Gunn & Peterson 1965]. This difference could be explained by a different count-binning or an updated XRT calibration used in our modeling.

The XRT light curve count rates have been converted to 1–10 keV fluxes using the results from our spectral modeling and calculating the ratio of the flux and count rate at the logarithmic center of the orbits. The 1–10 keV *Chandra* flux was derived using the actual spectral fit.

A broken power-law fit to the X-ray light curve results in $\alpha_1 = 1.16 \pm 0.06$, $\alpha_2 = 2.14 \pm 0.17$ and a break time of 110_{-23}^{+21} ks, or around 1.27 days. The difference between α_1 and α_2 and the fact that the spectral slope does not change across the break (the *Chandra* measurement is past the break) are highly indicative that the observed break in the light curve is a jet break. In § 3.1, we perform full modeling of the afterglow using the fireball model, indeed resulting in a jet-break time t_j that agrees reasonably well with the break time as determined from only the X-rays. We point out that our value for t_j is different from that cited in Racusin et al. (2005b) largely because their measurement of t_j was based on a preliminary XRT light curve.

2.2. Optical and Near-Infrared Observations

Observations were obtained in the *Z* and *R* bands with the William Herschel Telescope (WHT) using the Auxiliary Port and the Prime Focus Imaging Camera, respectively, in $r'i'z'$ with the Gemini South telescope using the GMOS instrument, in *JHK_s* with the Wide Field Camera on the United Kingdom Infrared Telescope (UKIRT), in *BVRI* with the DFOSC instrument on the Danish 1.54 m telescope, and in *J* and *K_s* with the Southern Astrophysical Research (SOAR) telescope using OSIRIS. The optical data were reduced in a standard fashion using the *ccdproc* package within the IRAF software (Tody 1986), whereas the SOAR data were reduced using the *cirred* package within IRAF. The UKIRT data were reduced using the standard pipeline reduction for WFCAM.

Photometric calibration was done using the calibration provided by Henden (2005) for Johnson-Cousins filters. For the $r'i'z'$ GMOS filters, we converted the magnitudes of the calibration stars provided by Henden to the Sloan filter system using the transformations provided by Jester et al. (2005) and verified by the published GMOS zero points. The WHT *Z* band was calibrated using the spectroscopic standard star SP 2323+157. Calibration of the infrared *JHK* magnitudes was done using the 2MASS catalog (Skrutskie et al. 2006).

No variable optical source was found at the position of the X-ray and radio afterglow. For the early epoch images (< 1 day

TABLE 1
OVERVIEW OF OPTICAL OBSERVATIONS

Start Date (UT)	ΔT (Average) (days)	Exposure Time (s)	Filter	Seeing (arcsec)	Telescope + Instrument
2005 Oct 22 23:25:14.....	0.4287	1800	<i>Z</i>	0.8	WHT + API
2005 Oct 23 00:22:33.....	0.4684	1620	<i>J</i>	1.2	SOAR + OSIRIS
2005 Oct 23 00:56:00.....	0.4917	1620	<i>K_s</i>	1.3	SOAR + OSIRIS
2005 Oct 23 00:48:03.....	0.5144	1920	<i>i'</i>	0.6	Gemini South + GMOS
2005 Oct 23 01:07:53.....	0.5288	1920	<i>r'</i>	0.6	Gemini South + GMOS
2005 Oct 23 01:27:46.....	0.5426	1920	<i>z'</i>	0.5	Gemini South + GMOS
2005 Oct 23 06:31:03.....	0.7525	720	<i>J</i>	1.4	UKIRT + WFCAM
2005 Oct 23 06:36:39.....	0.7526	360	<i>H</i>	1.3	UKIRT + WFCAM
2005 Oct 23 06:47:59.....	0.7604	360	<i>K</i>	1.3	UKIRT + WFCAM
2005 Oct 23 21:15:57.....	1.3389	1200	<i>Z</i>	1.0	WHT + API
2005 Oct 24 09:35:10.....	1.8467	720	<i>K</i>	0.3	UKIRT + WFCAM
2005 Oct 25 01:34:03.....	2.5181	1602	<i>K_s</i>	1.3	SOAR + OSIRIS
2005 Oct 25 02:13:18.....	2.5454	720	<i>J</i>	1.2	SOAR + OSIRIS
2005 Oct 25 02:22:02.....	2.5698	1920	<i>r'</i>	1.1	Gemini South + GMOS
2005 Oct 25 02:39:59.....	2.5792	1440	<i>z'</i>	1.2	Gemini South + GMOS
2005 Oct 26 00:36:58.....	3.4785	1800	<i>R</i>	1.4	WHT + PFIIP
2005 Oct 26 02:48:06.....	3.5695	600	Gunn <i>i</i>	1.4	DK 1.54 m + DFOSC
2005 Oct 26 03:23:35.....	3.5942	600	<i>R</i>	1.9	DK 1.54 m + DFOSC
2005 Oct 27 01:01:04.....	4.4952	600	<i>B</i>	2.3	DK 1.54 m + DFOSC
2005 Oct 27 02:00:48.....	4.5367	600	<i>V</i>	1.8	DK 1.54 m + DFOSC
2005 Oct 27 02:59:20.....	4.5773	600	<i>R</i>	1.6	DK 1.54 m + DFOSC
2005 Oct 28 02:18:38.....	5.5491	600	<i>i</i>	1.4	DK 1.54 m + DFOSC
2005 Oct 30 01:33:57.....	7.5180	600	<i>V</i>	1.4	DK 1.54 m + DFOSC
2005 Oct 30 02:32:59.....	7.5590	600	<i>B</i>	1.8	DK 1.54 m + DFOSC
2005 Oct 30 04:18:30.....	7.6323	600	<i>U</i>	1.8	DK 1.54 m + DFOSC
2005 Oct 31 01:03:40.....	8.4970	600	<i>R</i>	1.0	DK 1.54 m + DFOSC
2005 Oct 31 02:10:02.....	8.5431	600	<i>V</i>	1.0	DK 1.54 m + DFOSC
2005 Oct 31 03:19:05.....	8.5910	600	<i>B</i>	1.0	DK 1.54 m + DFOSC
2005 Nov 01 01:52:57.....	9.5312	600	<i>R</i>	0.9	DK 1.54 m + DFOSC
2005 Nov 02 02:04:47.....	10.539	600	<i>V</i>	1.2	DK 1.54 m + DFOSC
2005 Nov 03 01:10:34.....	11.502	600	<i>B</i>	1.2	DK 1.54 m + DFOSC
2005 Nov 07 01:25:30.....	15.512	600	Gunn <i>i</i>	1.4	DK 1.54 m + DFOSC
2005 Nov 08 01:40:48.....	16.523	600	Gunn <i>i</i>	1.4	DK 1.54 m + DFOSC

postburst), we estimated a limiting magnitude by performing image subtraction between this and a later image using the ISIS image subtraction package (Alard 2000). To this end, artificial low signal-to-noise ratio sources were added onto the images, with a Gaussian point-spread function (PSF) matched in size to the seeing (some artificial sources were added on top of existing sources, e.g., galaxies, some on the background sky). We determined our upper limit to be the point where we could retrieve 50% of the artificial sources in the subtracted image. This assumes that the change in brightness of any point source on top of the host galaxy is sufficient to be seen in such a subtracted image. With the difference in time between the epochs, this seems a reasonable assumption (for example, for a source fading with a shallow power-law-like slope of $F \propto t^{-0.5}$, the magnitude difference between the two WHT *Z*-band observations is ≈ 0.6 mag).

Photometry of the host galaxy has been performed using aperture photometry, with an aperture 1.5 times the seeing for each image, estimated from the measured FWHM of the PSF for point sources in the images.

Table 1 shows the log of our optical/NIR observations, while Table 2 shows the upper limits for any optical/NIR afterglow.

2.3. Radio Observations

Radio observations were performed with the WSRT at 8.4, 4.9, and 1.4 GHz. We used the Multi Frequency Front Ends (Tan 1991)

in combination with the IVC + DZB back end¹⁸ in continuum mode, with a bandwidth of 8×20 MHz. Gain and phase calibrations were performed with the calibrators 3C 286 and 3C 48, although at one 8.4 GHz measurement 3C 147 was used. Reduction and analysis were performed using the MIRIAD software package.¹⁹

¹⁸ See § 5.2 of the WSRT guide at <http://www.astron.nl/wsrt/wsrtGuide/node6.html>.

¹⁹ See <http://www.atnf.csiro.au/computing/software/miriad>.

TABLE 2
LIMITING MAGNITUDES

Filter	Limiting Magnitude ^a	ΔT (Average) (days)	Frequency (Hz)	Specific Flux ^b (μ Jy)
<i>K_s</i>	>20.0	0.4917	1.40×10^{14}	<6.82
<i>J</i>	>20.3	0.4684	2.40×10^{14}	<12.3
<i>Z</i>	>22.9	0.4287	3.43×10^{14}	<2.66
<i>z'</i>	>23.5	0.5426	3.36×10^{14}	<1.53
<i>r'</i>	>25.3	0.5288	4.76×10^{14}	<0.305

^a See text for the definition of the limiting magnitude.

^b Specific fluxes have been corrected for a Galactic extinction value of $E_{B-V} = 0.04$ (Schlegel et al. 1998) and converted from magnitudes using the calibration by Tokunaga & Vacca (2005) for the *JK_s* filters; the other filters are on the AB magnitude system (Oke & Gunn 1983).

TABLE 3
OVERVIEW OF WSRT RADIO OBSERVATIONS

Start Date (UT)	ΔT (Average) (days)	Integration Time (hr)	Frequency (GHz)	Specific Flux (μJy)
2005 Oct 23 15:20:10.....	1.19	5.0	4.9	281 \pm 32
2005 Oct 24 15:17:17.....	2.22	6.2	4.9	342 \pm 34
2005 Oct 25 15:12:58.....	3.30	5.4	4.9	143 \pm 30
2005 Oct 25 15:56:10.....	3.33	5.4	1.4	8 \pm 78
2005 Oct 28 18:33:08.....	6.40	8.5	4.9	91 \pm 28
2005 Oct 30 18:00:00.....	8.32	5.8	4.9	138 \pm 28
2005 Nov 01 18:00:00.....	10.38	8.9	4.9	169 \pm 28
2005 Nov 04 17:31:12.....	13.37	4.6	4.9	70 \pm 34
2005 Nov 04 18:14:24.....	13.37	4.0	8.5	38 \pm 132
2005 Nov 08 14:19:41.....	17.19	7.0	8.5	28 \pm 97

The observations are detailed in Table 3. In our modeling described in § 3.1 we have also used the VLA radio detection at 8.5 GHz from Cameron & Frail (2005).

3. ANALYSIS

3.1. Broadband Modeling

We have performed broadband modeling of the X-ray and radio measurements, using the methods presented in van der Horst et al. (2007). In our modeling we assume a purely synchrotron radiation mechanism.

The relativistic blast wave causing the afterglow accelerates electrons to relativistic velocities, which gives rise to a broadband spectrum with three characteristic frequencies: the peak frequency ν_m , corresponding to the minimum energy of the relativistic electrons that are accelerated by the blast wave; the cooling frequency ν_c , corresponding to the electron energy at which electrons lose a significant fraction of their energy by radiation on a timescale that is smaller than the dynamical timescale; and the self-absorption frequency ν_a , below which synchrotron self-absorption produces significant attenuation. The broadband spectrum is further characterized by the specific peak flux $F_{\nu, \text{max}}$ and the slope p of the electron energy distribution.

The dynamics of the relativistic blast wave determine the temporal behavior of the broadband synchrotron spectrum, i.e., the light curves at given frequencies. At first the blast wave is extremely relativistic, but is decelerated by the surrounding medium. When the Lorentz factor Γ of the blast wave becomes comparable to θ_j^{-1} , where θ_j is the opening angle of the jet, the jet starts to spread sideways. At that time, t_j , the temporal behavior of the broadband spectrum changes (see, e.g., Rhoads 1997).

We fit our data to six parameters: ν_c , ν_m , ν_a , $F_{\nu, \text{max}}$, p , and t_j . From these parameters and the redshift of the burst, $z = 0.8$, we can find the physical parameters governing the blast wave and its surroundings: the blast wave isotropic equivalent energy E_{iso} , the jet opening angle θ_j , the collimation corrected blast wave energy E_{jet} , the fractional energy densities behind the relativistic shock in electrons and in the magnetic field ϵ_e and ϵ_B , respectively, and the density of the surrounding medium. The meaning of the latter parameter depends on the density profile of the surrounding medium. For a homogeneous circumburst medium, we simply determine the density n . For a massive stellar wind, where the density is proportional to R^{-2} with R the distance to the GRB explosion center, we obtain the parameter A_* , which is the ratio of the mass-loss rate over the terminal wind velocity of the GRB progenitor.

Our modeling results are shown in Table 4, for both the homogeneous external medium and the stellar wind environment. The

light curves for the best-fit parameters are shown in Figure 1. We have performed Monte Carlo simulations with synthetic data sets in order to derive accuracy estimates of the best-fit parameters, which are also given in the table. It is evident from the results that our six-fit parameters are reasonably well constrained in both cases for the circumburst medium. The derived physical parameters are also well constrained, except for ϵ_e and ϵ_B . The values we find for both the isotropic and the collimation corrected energy are similar to those found for other bursts; this is also true for p (see, e.g., Panaitescu & Kumar 2001; Yost et al. 2003). The jet opening angle and the density of the surrounding medium are quite small, but neither are unprecedented. The jet-break time t_j is somewhat smaller than estimated in § 2.1, but both estimates have relatively large errors, likely because of the lack of (X-ray) data around the jet-break time.

With the absence of optical light curves, it is not possible to discriminate between the two different circumburst media. This is mainly due to the fact that the X-ray band lies above both ν_m and ν_c , in which case the slopes of the light curves do not depend on the density profile of the circumburst medium. (Even at 0.15 days, back-extrapolating ν_c from Table 4 results in its value being below the X-ray band.) The χ_{red}^2 is somewhat better for the stellar wind

TABLE 4
RESULTS OF BROADBAND MODELING FOR BOTH A HOMOGENEOUS
EXTERNAL MEDIUM AND A MASSIVE STELLAR WIND

Parameter	Homogeneous	Stellar Wind
$\nu_c(t_j)$ (Hz)	$(1.45^{+1.12}_{-0.23}) \times 10^{17}$	$(2.84^{+0.32}_{-1.30}) \times 10^{17}$
$\nu_m(t_j)$ (Hz).....	$(3.50^{+2.28}_{-1.47}) \times 10^{11}$	$(2.90^{+2.03}_{-1.15}) \times 10^{11}$
$\nu_a(t_j)$ (Hz).....	$(4.56^{+2.85}_{-3.08}) \times 10^9$	$(2.68^{+2.17}_{-1.60}) \times 10^9$
$F_{\nu, \text{max}}(t_j)$ (μJy).....	888^{+52}_{-109}	694^{+30}_{-240}
p	$2.06^{+0.19}_{-0.05}$	$2.10^{+0.08}_{-0.09}$
t_j (days).....	$0.96^{+0.40}_{-0.28}$	$1.06^{+0.41}_{-0.11}$
θ_j (deg).....	$3.39^{+2.02}_{-2.27}$	$2.30^{+1.09}_{-0.85}$
E_{iso} (erg).....	$(5.23^{+1.13}_{-1.69}) \times 10^{52}$	$(28.2^{+31.0}_{-10.4}) \times 10^{52}$
E_{jet} (erg).....	$(0.917^{+0.655}_{-0.512}) \times 10^{50}$	$(2.27^{+2.25}_{-0.79}) \times 10^{50}$
ϵ_e	$0.247^{+1.396}_{-0.212}$	$0.0681^{+0.3951}_{-0.0348}$
ϵ_B	$(7.63^{+42.57}_{-6.30}) \times 10^{-3}$	$(8.02^{+28.18}_{-7.17}) \times 10^{-3}$
n (cm^{-3}).....	$(1.06^{+9.47}_{-1.04}) \times 10^{-2}$...
A_*^a	$(2.94^{+6.98}_{-2.11}) \times 10^{-2}$
χ_{red}^2	1.9	1.5

NOTES.—The best-fit parameters are shown together with accuracy estimates from Monte Carlo simulations with synthetic data sets. The characteristic frequencies of the synchrotron spectrum and the specific peak flux are given at t_j .

^a The parameter A_* is a measure for the density in the case of a stellar wind environment, being the ratio of the mass-loss rate over the terminal wind velocity, here given in units of $10^{-5} M_{\odot} \text{ yr}^{-1}$ divided by a wind velocity of 1000 km s^{-1} (see van der Horst et al. 2007).

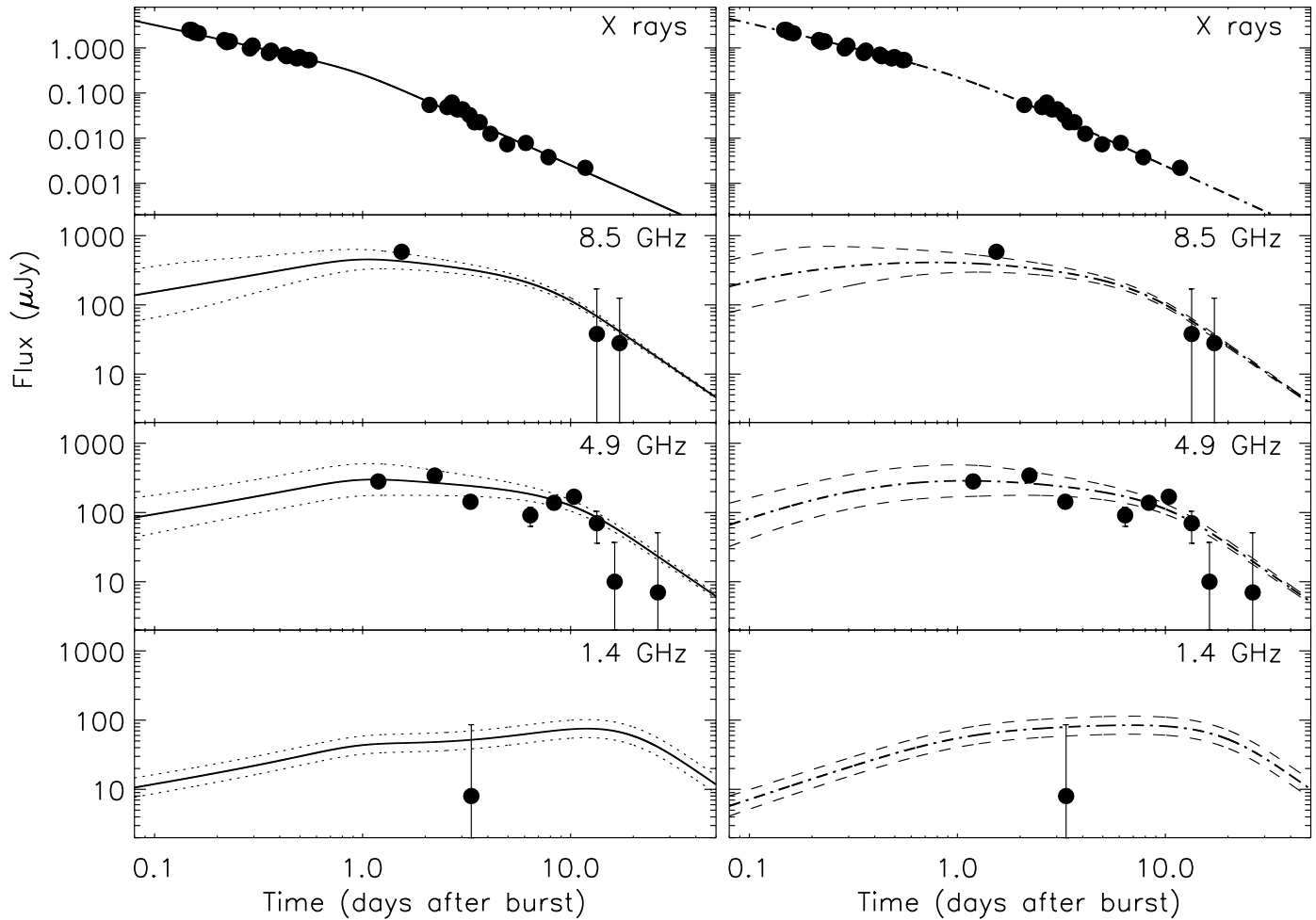


FIG. 1.—Fit results for a homogeneous circumburst medium (*left*) and a massive stellar wind (*right*). The solid and dash-dotted lines are the best model fits, and the dotted and dashed lines indicate the predicted rms scatter due to interstellar scintillation; see the Appendix for further details. Also included in the figure (and modeling) is the reported VLA 8.5 GHz detection (Cameron & Frail 2005; *leftmost point in the 8.5 GHz subplot*).

case, but the homogeneous case cannot be excluded. From the X-ray light curve, however, one can conclude that the density profile of the medium does not change between approximately 0.15 and 12 days after the burst. If there were a transition from a stellar wind to a homogeneous medium, the X-ray flux would have to rise or drop significantly, unless the densities are fine-tuned at the transition point (Pe'er & Wijers 2006). From the fact that the medium does not change during the X-ray observations, one can draw conclusions on the distance of the wind termination shock of the massive star: if one assumes that the medium is already homogeneous at ≈ 0.15 days, the wind termination shock position is at $R_w \lesssim 9.8 \times 10^{17}$ cm (0.32 pc); if the circumburst medium is a stellar wind up to ≈ 12 days after the burst, $R_w \gtrsim 1.1 \times 10^{19}$ cm (3.7 pc).

3.2. The Nondetection of the Optical Afterglow

It is quickly seen that GRB 051022 falls into the category of the so-called dark bursts. Using, for example, the quick criterion proposed by Jakobsson et al. (2004) we find $\beta_{\text{ox}} < -0.05$ at 12.7 hr after the burst using the Gemini r' -band observation, well below the proposed limit of $\beta_{\text{ox}} < 0.5$. A more precise criterion would combine the available spectral and temporal parameters of the X-ray afterglow, allow all valid combinations, and from that imply the range of possible optical magnitudes from the X-rays (see, e.g., Rol et al. 2005). This is, in fact, implied in our previous modeling: the modeled specific fluxes corresponding to the band and

epoch of our optical and NIR upper limits are listed in Table 5 (see also Table 2).

While the values in this table are given for local extinction, not K -corrected to $z = 0.8$, it is immediately obvious that our K -band observations put a stringent constraint on the required extinction directly surrounding the burst.

To estimate the amount of local extinction in the host galaxy, we have modeled the NIR to X-ray spectrum around 0.5 days after the burst, considering three different extinction curves: those of the Milky Way (MW), the Large Magellanic Cloud (LMC), and the Small Magellanic Cloud (SMC), from Pei (1992), with R_V of 3.08, 3.16, and 2.93, respectively.

For this, we used the unabsorbed XRT flux obtained from the spectral fit to orbits 3–7 (which do not contain piled-up data) and fixed the energy spectral slope in the X-rays at $\beta = 1$ (also from the X-ray spectral fit). The optical specific fluxes were scaled to the logarithmic midobservation time of the X-ray observations with an assumed $\alpha = 1.16$ decline. This estimated optical decay is derived from the prebreak X-ray decay value, allowing for the cooling break between the two wavelength regions and averaging the two possible values for $\alpha_X - \alpha_{\text{opt}}$ (-0.25 and 0.25). We can further put the most stringent constraint on the broken power-law spectral shape, by setting the spectral break just below the X-rays, at 1.8×10^{17} Hz, which follows from our previous broadband modeling. Our results indicate that, for the aforementioned

TABLE 5
UPPER LIMITS COMPARED TO MODEL SPECIFIC FLUX CALCULATIONS

FILTER	UPPER LIMIT (μJy)	HOMOGENEOUS DENSITY PROFILE			STELLAR WIND DENSITY PROFILE		
		Modeled Specific Flux (μJy)	Extinction (mag)	E_{B-V}	Modeled Specific Flux (μJy)	Extinction (mag)	E_{B-V}
K_s	<6.82	93.1	2.84	7.74	57.2	2.31	6.29
J	<12.3	117	2.44	2.71	74.1	1.95	2.16
Z	<2.66	103	3.97	2.58	67.8	3.52	2.29
r'	<0.305	74.5	5.97	2.17	44.4	5.41	1.97
z'	<1.53	87.7	4.40	2.97	51.9	3.83	2.59

NOTES.—The inferred lower limits on the extinction are given in the observer frame. The E_{B-V} values are given for a Galactic extinction curve ($R_V = 3.08$) and are for illustrative purposes; see the comments at the end of § 3.2.

extinction curves, a local extinction of $E_{B-V} \approx 7$ (for all three extinction curves) is necessary to explain the K -band upper limit.

We can relate the resulting N_H from our X-ray spectral fits to any local E_{B-V} , using the relations found in Predehl & Schmitt (1995), Fitzpatrick (1985), and Martin et al. (1989) for $N(\text{H I})/E_{B-V}$, and adjusting the metallicity in our X-ray absorption model accordingly. We obtain $E_{B-V} = 7.5, 1.54,$ and 0.84 for a MW, LMC, and SMC extinction curve, respectively, with the MW value showing the best agreement with our findings for optical extinction. (Both Nakagawa et al. [2006] and Butler et al. [2005b] find E_{B-V} values roughly twice as high here, for a MW extinction curve only, since their N_H estimate is larger than ours.) This, obviously, depends on the assumption that the MW (or otherwise, LMC or SMC) extinction curves are valid models to compare with our observed data here. Since these data happen to originate from just one sight line in a galaxy, this may very well not be the case. Furthermore, even if the extinction curve is correct, the actual value of R_V may be rather different for the host galaxy. Finally, the E_{B-V} - N_H relations show a rather large scatter, especially at higher column densities, and the N_H is not always derived using X-ray spectroscopy. Our above results are therefore approximations, which are useful to compare with other (GRB host) studies, but should be taken with the necessary caution.

3.3. The Host Galaxy of GRB 051022

Using the optical data described above, we fit the SED of the host of GRB 051022 using the HyperZ program²⁰ developed by

²⁰ See <http://webast.ast.obs-mip.fr/hyperz>.

TABLE 6
MEASURED HOST-GALAXY MAGNITUDES

Filter	Magnitude	Magnitude Error
K	18.40	0.04
K_s	18.36	0.09
H	19.42	0.09
J	19.92	0.05
Z^a	21.41	0.05
z'	21.30	0.04
i'	21.77	0.01
r'	22.04	0.01
R	21.84	0.09
V	22.30	0.04
B	22.75	0.02
U	> 21.3 ^b	...

^a AB magnitude.

^b 5σ upper limit.

Bolzonella et al. (2000). The photometry of the host has been performed using `apphot` within IRAF, in an aperture 1.5 times the estimated seeing in the different exposures. The results are reported in Table 6 (see also Ovaldsen et al. 2007). The range of photometric magnitudes reported in this paper provides one of the most complete broadband optical data sets of a GRB host galaxy to date. We fit using the eight synthetic galaxy templates provided within HyperZ at the redshift of the host and find that the host galaxy is a blue compact galaxy of type irregular, with a dominant stellar population age of ≈ 20 Myr, similar to other long GRB hosts (Christensen et al. 2005). A moderate amount of extinction of $A_V \approx 1$ mag is required to fit the SED, with an SMC-type extinction curve providing a best fit, and the luminosity of the host is approximately $1.5L_*$ (assuming $M_{*,B} = -21$); these findings are in full agreement with Castro-Tirado et al. (2006). The amount of extinction in the line of sight toward the GRB required to suppress the optical light of the afterglow to the observed limits is clearly higher than the A_V value found from the host SED: $A_V = 4.4$ mag toward the GRB, estimated from blue-shifting our measured (observer frame) z' -band extinction to $z = 0.8$. The host-galaxy SED extinction is, however, an average value derived from the integrated colors of the host.

The host of GRB 051022 is located in a field crowded with galaxies of various Hubble types. We perform photometry on several galaxies close to the GRB host (within $1'$) to investigate the possibility that the high star formation rate seen in the optical (Castro-Tirado et al. [2006] report an SFR of $\approx 20 M_\odot \text{ yr}^{-1}$) is induced by a recent interaction with one of the neighboring galaxies. As formation of high-mass stars has also been observed to occur in dusty regions in merging systems (see, e.g., Lin et al. 2007), this could help to explain the excess optical extinction toward GRB 051022. We performed HyperZ fits to these galaxies and found that none of them are well fit by a photometric redshift of $z \approx 0.8$. In particular, the two galaxies closest to the GRB host galaxy are not compatible with a redshift 0.8 and show best fits with photometric redshifts of $z \approx 0.2-0.25$. Out of the sample of six galaxies close to the GRB host we find that four have best-fit photometric redshifts in the range 0.20–0.25, making it unlikely that a possible overdensity of galaxies near the host galaxy is due to a cluster or galaxy group at the host redshift.

4. DISCUSSION

The issue of nondetected (“dark”) GRB afterglows has received significant interest ever since the discovery of the first GRB afterglow, starting with the nondetection of GRB 970828 to very deep limits (Groot et al. 1998; Odewahn et al. 1997). For this particular afterglow, its nondetection has been attributed to a dust lane in its host galaxy (Djorgovski et al. 2001). Dust extinction as the

cause of the nondetection of the optical afterglow has been inferred in the case of several other GRBs, notably those with a precise X-ray or radio position, where one can pinpoint the afterglow position on top of its host galaxy (e.g., GRB 000210; Piro et al. 2002).

Optical drop-outs due to high redshift will also result in dark bursts, but they are harder to confirm, since it would require at least one detection in a red band to detect the Ly α break. Otherwise, it becomes indistinguishable from dust extinction.

Other explanations of afterglow nondetections include the intrinsic faintness of the afterglow. For *HETE-2* detected GRBs, this has been inferred for, e.g., GRB 020819 (Jakobsson et al. 2005). For *Swift* bursts, where rapid and accurate X-ray positions are often available, this is a major cause of nondetections (Berger et al. 2005), largely attributed to a higher average redshift.

In our case here, the host galaxy has been detected at a relatively modest redshift, which almost automatically points to the dust extinction scenario. The radio and X-ray detections even allow us to accurately model the necessary amount of extinction between us and the GRB.

4.1. The Burst Environment

The issue of the role of dust extinction in the lines of sight toward GRBs is still very much an open one. While clear signs of dust depletion are seen in several afterglow spectra, the A_V values that are predicted from these depletion measures are generally much higher than the observed ones, which can be found from the continuum shape (Savaglio & Fall 2004). Recently, selected samples of GRB afterglows were homogeneously analyzed for X-ray and optical extinction, showing dust-to-gas ratios different from Galactic and Magellanic Cloud values (Starling et al. 2007; Schady et al. 2007). Galama & Wijers (2001) and Stratta et al. (2004) had already found dust (optical) to gas (X-ray) ratios to be lower than the Galactic value (in all cases, however, there is a bias in these samples to optically and X-ray detected afterglows). Comparison of neutral hydrogen columns and metallicities of afterglow lines of sight with X-ray extinction values (Watson et al. 2007) showed that the absorption probed by these two wavelength regimes is generally located at different positions in the host. In all these cases there may be significant but hard to quantify biases against bursts with low apparent magnitudes, thereby preventing optical spectroscopy.

In the case of GRB 051022 there is a significant discrepancy between the extinction for the host as a whole and that along the line of sight to the burst, or at least along our line of sight toward the burst. This is perhaps not too surprising if one assumes, for example, that the burst occurred inside a giant molecular cloud (GMC). Jakobsson et al. (2006a) compared the GRB $N(\text{H I})$ distribution to that of modeled GRBs located inside Galactic-like GMCs. They found that the two distributions are incompatible, and GRBs are possibly more likely to occur inside clouds with a lower $N(\text{H I})$, or alternatively, outside the actual GMC. (Note that their study concentrates on bursts with $z > 2$, where the Ly α absorption is visible in the optical wave bands; it is also biased toward optically detected afterglows.) A GMC could therefore actually be positioned in front of the GRB, where the required optical and X-ray extinction is easily achieved. This agrees with the findings by Prochaska et al. (2007), who analyzed several GRB damped Ly α spectra and from observed depletion levels infer that the gas is not located directly near the GRB (e.g., its molecular cloud) but farther out. The specific case of GRB 060418 confirmed this through time-resolved high-resolution spectroscopy,

showing that the observed metal lines originate past 1.7 kpc from the burst itself (Vreeswijk et al. 2007). In fact, X-ray radiation from the burst could easily destroy grains out to 100 pc (Waxman & Draine 2000; Fruchter et al. 2001; Draine & Hao 2002) and permit the afterglow radiation to penetrate the surrounding molecular cloud. Dust extinction is therefore likely to occur farther out, perhaps to several kiloparsecs.

It is interesting to find a non-SMC type of extinction curve from the combination of X-ray and optical absorption (although it is not completely ruled out): in most cases modeled, an SMC extinction curve fits the optical–X-ray spectra best (Starling et al. 2007; Schady et al. 2007), presumably attributable to the absence of the 2175 Å feature (Savage & Mathis 1979) and the low dust-to-gas ratio. Our findings indicate that the extinction along the line of sight to the GRB will generally be different from one of the three assumed extinction curves. Local small-scale density variations in clouds, such as found by infrared studies in the Taurus region and from simulations (Padoan et al. 2006), could cause this fairly easily.

4.2. Energetics

Our modeling provides us with a detailed set of parameters of the afterglow energetics, including E_{jet} , the energy of the afterglow. For the prompt emission energy, we use the data from the *Konus-Wind* measurements (Golenetskii et al. 2005). We calculate a prompt isotropic energy of $4.39^{+0.29}_{-0.18} \times 10^{53}$ erg in the 20 keV to 20 MeV observer frame and, by applying a K -correction (as in, e.g., Bloom et al. 2001), $E_{p,\text{iso}} = 10.4^{+0.7}_{-0.4} \times 10^{53}$ erg in the 1–10⁵ keV rest frame. The collimation corrected energy depends on the assumed density profile of the surrounding medium: for a homogeneous medium, we obtain $E_{p,\text{jet}} = 18.2 \times 10^{50}$ erg, and for a wind-like medium, $E_{p,\text{jet}} = 8.38 \times 10^{50}$ erg. With $E_{\text{peak}} = 918^{+66}_{-59}$ keV in the burst rest frame, we find that the $E_{\text{peak}}-E_{p,\text{jet}}$ relation (Ghirlanda et al. 2004) somewhat underestimates the E_{peak} when calculated from $E_{p,\text{jet}}$: $E_{\text{peak}} \approx 740$ keV for a homogeneous medium and ≈ 430 keV for a wind medium. (The difference between our chosen cosmology and that used by Ghirlanda et al. [2004] amounts to only a 0.3% difference in E_{iso} .) These estimates, however, come with a few caveats: (1) The E_{peak} from the *Konus-Wind* data is calculated using an exponential cutoff model, not the Band function (Band et al. 1993). But since the Band function includes the case of an exponential cutoff model (with $\beta = -\infty$), this should pose no problem in estimating the actual E_{peak} . (2) Our break time, and therefore the jet-opening angle, is calculated from the full modeling of the afterglow, which effectively means derived from the available X-ray and radio data. Furthermore, the original Ghirlanda relation was derived using optical break times. Recent efforts show that estimating jet-break times from X-ray light curves may not lead to the same results (e.g., Panaitescu et al. 2006). Finally, (3) the relatively large error on the jet opening angle estimate allows for a relatively large range in collimation corrected energies. We have simply used here our best value, but an E_{peak} value of 1498 keV derived from E_{jet} can still be accommodated within our errors. (We note that, with a different E_{peak} estimate and an incorrect value for the jet-break time, Nakagawa et al. 2006 still found their results to lie on the Ghirlanda relation.) The break time problem can be avoided by looking only at the $E_{\text{peak}}-E_{p,\text{iso}}$ relation (Amati et al. 2002; Amati 2006). From this, we estimate $E_{\text{peak}} \approx 924$ keV, nicely in agreement with the value found directly from the spectra fit.

Comparing the prompt emission energy ($E_{p,\text{jet}}$) and afterglow blast wave kinetic energy (E_{jet}), we find their ratio to be

$E_{p,\text{jet}}/E_{\text{jet}} = 3.7$ in the case of a windlike circumburst medium, while for a homogeneous medium, $E_{p,\text{jet}}/E_{\text{jet}} = 20$. These ratios are similar to those found for other bursts (e.g., Berger et al. 2003, Fig. 3).

GRB 051022 is also one of the brightest bursts observed by *HETE-2*, with a prompt 30–400 keV fluence of $S = 1.31 \times 10^{-4}$ erg cm $^{-2}$ (Nakagawa et al. 2006). In fact, compared to the sample of 35 FREGATE bursts analyzed by Barraud et al. (2003) GRB 051022 has the largest fluence, even topping the relatively close by GRB 030329 ($S = 1.2 \times 10^{-4}$ erg cm $^{-2}$ [Vanderspek et al. 2004]; note that for GRB 051022, its redshift is close to the median redshift of *HETE-2* detected GRBs and therefore distance effects will play a very minor role). Rol et al. (2005) noted this potential correlation of fluence with the nondetection of a GRB afterglow for the small subset of genuinely dark bursts in their sample: the truly dark bursts all have a much higher than average fluence (although this is for a relatively small sample only). Potentially, this could point to an external origin for the prompt emission, instead of being due to internal shocks: a large amount of dust may result in more matter that will radiate, while at the same time the radiation will be suppressed at UV and optical wavelengths. This would indicate an origin of the extinction quite close to the burst instead, in contrast to previous findings for other bursts, as discussed in § 4.1. These latter bursts, however, were all optically selected to obtain spectroscopy and may therefore show surroundings different from those of GRB 051022. Unfortunately, with the small sample size of genuine dark bursts a firm conclusion on this correlation is not possible, but it remains something to watch for in future dark bursts.

5. CONCLUSIONS

GRB 051022 is a prototypical dark burst, with the local extinction exceeding 2.3 mag in *J* and 5.4 mag in *U*, in the host-galaxy rest frame, with the exact limits depending on the circumburst density profile. The extinction curve derived from an X-ray–optical spectral fit points toward a Galactic type of extinction curve, although it is likely that this is more or less a coincidence: the host galaxy itself is best modeled with an SMC-like extinction curve, with a modest amount of extinction, $A_V \approx 1$ mag. The large optical absorption toward the afterglow of GRB 051022 is therefore probably the effect of an unfortunate position in the host where the line of sight crosses dense regions within the host.

The X-ray and radio afterglow data allow for a full solution of the blast wave model, although we unfortunately cannot distinguish between the density profile (homogeneous or windlike) of the circumburst medium. We estimate a collimation corrected energy in the afterglow emission of $(0.92\text{--}2.3) \times 10^{50}$ erg, while the energy in prompt emission (1–10 5 keV rest frame) is $(8.4\text{--}18) \times 10^{50}$ erg. Aside from the large optical extinction, the afterglow otherwise appears as an average afterglow, with no outstanding

properties. The potentially interesting point here is that the 30–400 keV fluence of the prompt emission is one of the largest ever detected in the *HETE-2* sample.

In the era of *Swift* GRBs, dust-extincted bursts can actually be found in optical/NIR thanks to the rapid availability of precise positions: examples are found where the burst is relatively bright early on at optical/NIR wavelengths, while the afterglow proper (after a few hours) often can go undetected (e.g., Oates et al. 2006; Perley et al. 2007). This allows targeted follow-up of such dark bursts, i.e., determining the host galaxy (and the burst’s precise position therein) and a redshift measurement. In our case, a precise *Chandra* and radio position pinpointed the host galaxy, but such data may not always be available. High-resolution late-time observations of the host, at the location of the GRB, may then reveal whether the burst indeed occurred inside a dense host region.

We thank the referee for a careful reading of the manuscript and constructive comments. We thank Kim Page and Andy Beardmore for useful discussions regarding the XRT data analysis. E. R. and R. L. C. S. acknowledge support from PPARC. K. W. and R. A. M. J. W. acknowledge support of NWO under grant 639.043.302. The authors acknowledge funding for the *Swift* mission in the UK by STFC, in the USA by NASA, and in Italy by ASI. The Dark Cosmology Centre is funded by the Danish National Research Foundation. The William Herschel Telescope is operated on the island of La Palma by the Isaac Newton Group in the Spanish Observatorio del Roque de los Muchachos of the Instituto de Astrofísica de Canarias. The United Kingdom Infrared Telescope is operated by the Joint Astronomy Centre on behalf of the UK Particle Physics and Astronomy Research Council. The data reported here were obtained as part of the UKIRT Service Programme. The Westerbork Synthesis Radio Telescope is operated by ASTRON (Netherlands Foundation for Research in Astronomy) with support from the Netherlands Foundation for Scientific Research (NWO). Support for this work was provided by the National Aeronautics and Space Administration through *Chandra* Award 1736937 issued by the *Chandra X-Ray Observatory* Center, which is operated by the Smithsonian Astrophysical Observatory for and on behalf of the National Aeronautics Space Administration under contract NAS8-03060. This publication makes use of data products from the Two Micron All Sky Survey, which is a joint project of the University of Massachusetts and the Infrared Processing and Analysis Center/California Institute of Technology, funded by the National Aeronautics and Space Administration and the National Science Foundation. This research has made use of data obtained from the High Energy Astrophysics Science Archive Research Center (HEASARC), provided by NASA’s Goddard Space Flight Center.

APPENDIX

INTERSTELLAR SCINTILLATION IN THE RADIO MODELING

The 4.9 GHz measurements show scatter around the best-fit light curve, which can be accounted for by interstellar scintillation (ISS). In Figure 1 we have indicated the predicted rms scatter due to ISS. We have calculated the scattering measure (SM) from the Cordes & Lazio (2002) model for the Galactic distribution of free electrons: $SM = 2.04 \times 10^{-4}$ kpc (m $^{-20/3}$) $^{-1}$. The radio specific flux will be modulated when the source size is close to one of the three characteristic angular scales, i.e., for weak, refractive, or diffractive ISS. From Walker (1998) we calculate the transition frequency between weak and strong ISS, $\nu_0 = 9.12$ GHz, and the angular size of the first Fresnel zone, $\theta_{F_0} = 0.994$ μ as. Our measurements were all performed at frequencies below ν_0 , i.e., in the strong ISS regime, which means that only refractive and diffractive ISS modulate the specific flux significantly. We calculate the evolution of the source size in the extreme

relativistic phase ($\theta_s = R/\Gamma$) and after the jet break ($\theta_s = R\theta_j$), and compare this source size with the diffractive angular scale $\theta_d = \theta_{F_0}(\nu_0/\nu)^{-6/5} = 0.0701\nu_{\text{GHz}}^{6/5} \mu\text{as}$ and the refractive angular scale $\theta_r = \theta_{F_0}(\nu_0/\nu)^{11/5} = 128\nu_{\text{GHz}}^{-11/5} \mu\text{as}$ to calculate the modulation index m_p . In the case of diffractive ISS the modulation index is 1, and in the case of refractive ISS $m_p = (\nu_0/\nu)^{-17/30} = 0.286\nu_{\text{GHz}}^{17/30}$. Because of the expansion of the blast wave the angular source size exceeds one of the characteristic angular scales at some point in time. Then the modulation will begin to quench as $m_p(\theta_d/\theta_s)$ in the case of diffractive ISS and as $m_p(\theta_r/\theta_s)^{7/6}$ in the case of refractive ISS.

REFERENCES

- Alard, C. 2000, A&AS, 144, 363
 Amati, L. 2006, MNRAS, 372, 233
 Amati, L., et al. 2002, A&A, 390, 81
 Arnaud, K. A. 1996, in ASP Conf. Ser. 101, Astronomical Data Analysis Software and Systems V, ed. G. H. Jacoby & J. Barnes (San Francisco: ASP), 17
 Band, D., et al. 1993, ApJ, 413, 281
 Barraud, C., et al. 2003, A&A, 400, 1021
 Berger, E., & Wyatt, P. 2005, GCN Circ. 4148, <http://gcn.gsfc.nasa.gov/gcn/4148.gcn3>
 Berger, E., et al. 2005, ApJ, 634, 501
 ———. 2003, Nature, 426, 154
 Bloom, J. S., Frail, D. A., & Sari, R. 2001, AJ, 121, 2879
 Bolzonella, M., Miralles, J.-M., & Pelló, R. 2000, A&A, 363, 476
 Bremer, M., Castro-Tirado, A. J., & Neri, R. 2005, GCN Circ. 4157, <http://gcn.gsfc.nasa.gov/gcn/gcn3/4157.gcn3>
 Butler, N. R., et al. 2005a, GCN Circ. 4165, <http://gcn.gsfc.nasa.gov/gcn/gcn3/4165.gcn3>
 ———. 2005b, GCN Circ. 4170, <http://gcn.gsfc.nasa.gov/gcn/gcn3/4170.gcn3>
 Cameron, P. B., & Frail, D. A. 2005, GCN Circ. 4154, <http://gcn.gsfc.nasa.gov/gcn/gcn3/4154.gcn3>
 Castro-Tirado, A. J., et al. 2006, A&A, in press (arXiv:0708.3043)
 Christensen, L., Hjorth, J., & Gorosabel, J. 2005, ApJ, 631, L29
 Cordes, J. M., & Lazio, T. J. W. 2002, preprint (astro-ph/0207156)
 Dickey, J. M., & Lockman, F. J. 1990, ARA&A, 28, 215
 Djorgovski, S. G., et al. 2001, ApJ, 562, 654
 Draine, B. T., & Hao, L. 2002, ApJ, 569, 780
 Evans, P. A., et al. 2007, A&A, 469, 379
 Fitzpatrick, E. L. 1985, ApJ, 299, 219
 Fruchter, A., Krolik, J. H., & Rhoads, J. E. 2001, ApJ, 563, 597
 Fynbo, J. U., et al. 2001, A&A, 369, 373
 Galama, T. J., & Wijers, R. A. M. J. 2001, ApJ, 549, L209
 Gal-Yam, A., et al. 2005, GCN Circ. 4156, <http://gcn.gsfc.nasa.gov/gcn/gcn3/4156.gcn3>
 Ghirlanda, G., Ghisellini, G., & Lazzati, D. 2004, ApJ, 616, 331
 Golenetskii, S., et al. 2005, GCN Circ. 4150, <http://gcn.gsfc.nasa.gov/gcn/gcn3/4150.gcn3>
 Groot, P. J., et al. 1998, ApJ, 493, L27
 Gunn, J. E., & Peterson, B. A. 1965, ApJ, 142, 1633
 Haislip, J. B., et al. 2006, Nature, 440, 181
 Henden, A. 2005, GCN Circ. 4184, <http://gcn.gsfc.nasa.gov/gcn/gcn3/4184.gcn3>
 Jakobsson, P., et al. 2004, ApJ, 617, L21
 ———. 2005, ApJ, 629, 45
 ———. 2006a, A&A, 460, L13
 ———. 2006b, A&A, 447, 897
 Jester, S., et al. 2005, AJ, 130, 873
 Levan, A., et al. 2006, ApJ, 647, 471
 Lin, L., et al. 2007, ApJ, 660, L51
 Martin, N., Maurice, E., & Lequeux, J. 1989, A&A, 215, 219
 Nakagawa, Y. E., et al. 2006, PASJ, 58, L35
 Oates, S. R., et al. 2006, MNRAS, 372, 327
 Odewahn, S. C., et al. 1997, IAU Circ. 6735, 1
 Oke, J. B., & Gunn, J. E. 1983, ApJ, 266, 713
 Olive, J., et al. 2005, GCN Circ. 4131
 Ovaldsen, J.-E., et al. 2007, ApJ, 662, 294
 Padoan, P., et al. 2006, ApJ, 649, 807
 Panaitescu, A., & Kumar, P. 2001, ApJ, 560, L49
 Panaitescu, A., et al. 2006, MNRAS, 369, 2059
 Patel, S., Kouveliotou, C., & Rol, E. 2005, GCN Circ. 4163, <http://gcn.gsfc.nasa.gov/gcn/gcn3/4163.gcn3>
 Pe'er, A., & Wijers, R. A. M. J. 2006, ApJ, 643, 1036
 Pei, Y. C. 1992, ApJ, 395, 130
 Perley, D. A., et al. 2007, ApJ, submitted (astro-ph/0703538)
 Piro, L., et al. 2002, ApJ, 577, 680
 Predehl, P., & Schmitt, J. H. M. M. 1995, A&A, 293, 889
 Prochaska, J. X., Chen, H.-W., Dessauges-Zavadsky, M., & Bloom, J. S. 2007, ApJ, submitted
 Racusin, J., Burrows, D., & Gehrels, N. 2005a, GCN Circ. 4141, <http://gcn.gsfc.nasa.gov/gcn/gcn3/4141.gcn3>
 Racusin, J., et al. 2005b, GCN Circ. 4169, <http://gcn.gsfc.nasa.gov/gcn/gcn3/4169.gcn3>
 Rhoads, J. E. 1997, ApJ, 487, L1
 Ricker, G. R., et al. 2003, in AIP Conf. Ser. 662, Gamma-Ray Burst and Afterglow Astronomy 2001: A Workshop Celebrating the First Year of the HETE Mission, ed. G. R. Ricker & R. K. Vanderspek (Mellville: AIP), 3
 Rol, E., Wijers, R. A. M. J., Kouveliotou, C., Kaper, L., & Kaneko, Y. 2005, ApJ, 624, 868
 Rol, E., et al. 2007, MNRAS, 374, 1078
 Savage, B. D., & Mathis, J. S. 1979, ARA&A, 17, 73
 Savaglio, S., & Fall, S. M. 2004, ApJ, 614, 293
 Schady, P., et al. 2007, MNRAS, 377, 273
 Schaefer, B. E. 2005, GCN Circ. 4132, <http://gcn.gsfc.nasa.gov/gcn/gcn3/4132.gcn3>
 Schlegel, D. J., Finkbeiner, D. P., & Davis, M. 1998, ApJ, 500, 525
 Skrutskie, M. F., et al. 2006, AJ, 131, 1163
 Starling, R. L. C., et al. 2007, ApJ, 661, 787
 Stratta, G., Fiore, F., Antonelli, L. A., Piro, L., & De Pasquale, M. 2004, ApJ, 608, 846
 Tan, G. H. 1991, in IAU Colloq. 131, Radio Interferometry: Theory, Techniques, and Applications, ed. T. J. Cornwell & R. A. Perley (ASP Conf. Ser. 19; San Francisco: ASP), 42
 Tanvir, N. R., et al. 2004, MNRAS, 352, 1073
 Tody, D. 1986, Proc. SPIE, 627, 733
 Tokunaga, A. T., & Vacca, W. D. 2005, PASP, 117, 421
 Torii, K. 2005, GCN Circ. 4130, <http://gcn.gsfc.nasa.gov/gcn/gcn3/4130.gcn3>
 Trentham, N., Ramirez-Ruiz, E., & Blain, A. W. 2002, MNRAS, 334, 983
 van der Horst, A., Wijers, R. A. M. J., & van der Horn, L. 2007, A&A, submitted
 van der Horst, A. J., Rol, E., & Wijers, R. A. M. J. 2005, GCN Circ. 4158, <http://gcn.gsfc.nasa.gov/gcn/gcn3/4158.gcn3>
 Vanderspek, R., et al. 2004, ApJ, 617, 1251
 Vreeswijk, P. M., et al. 2007, A&A, 468, 83
 Walker, M. A. 1998, MNRAS, 294, 307
 Watson, D., et al. 2007, ApJ, 660, L101
 Waxman, E., & Draine, B. T. 2000, ApJ, 537, 796
 Yost, S. A., Harrison, F. A., Sari, R., & Frail, D. A. 2003, ApJ, 597, 459